International Journal of Fatigue 33 (2011) 194–202

Contents lists available at ScienceDirect

International Journal of Fatigue

journal homepage: www.elsevier.com/locate/ijfatigue

Mechanisms and modelling of fatigue crack growth under combined low and high cycle fatigue loading

C. Schweizer *, T. Seifert, B. Nieweg, P. von Hartrott, H. Riedel

Fraunhofer Institute for Mechanics of Materials IWM, Woehlerstrasse 11, 79108 Freiburg, Germany

ARTICLE INFO

Article history:
Received 17 February 2010
Received in revised form 30 July 2010
Accepted 6 August 2010
Available online 13 August 2010

Keywords:
Low cycle fatigue
High cycle fatigue
Crack-tip opening displacement (CTOD)
Threshold stress intensity factor
Fatigue crack growth

ABSTRACT

In this paper a mechanism-based model is presented, which is able to describe the evolution of microcracks under pure low cycle fatigue (LCF) and combined LCF and high cycle fatigue (HCF) loading conditions. In order to verify the model and to calibrate the model parameters, the crack length evolution of microcracks is followed at room temperature for pure LCF and combined LCF/HCF loading in a 10%-chromium steel. These studies reveal accelerated crack growth rates under LCF/HCF interaction as soon as a critical crack length is reached. The model is capable of accounting for this effect and needs only few parameters, including the threshold for fatigue crack growth, whose knowledge is crucial for the accuracy of the model.

1. Introduction

Many engineering components are subjected to combined low cycle fatigue (LCF) and high cycle fatigue (HCF) loadings, e.g. LCF start–stop temperature cycles (thermomechanical fatigue, TMF) in steam turbine rotors are superimposed by HCF reverse bending cycles or vibrations. In combustion engines, combustion pressure results in superimposed HCF.

In the LCF regime larger strain amplitudes lead to early microcrack initiation, such that the component's lifetime is determined by the growth of these microcracks. The superimposed HCF cylces with smaller strain amplitudes even below the endurance limit of the respective material can reduce lifetimes significantly.

Several studies on aluminium and cobalt alloys, which were tested under combined TMF and HCF loading, showed that out-of-phase TMF lives are reduced with rising HCF amplitudes [1–3]. A higher frequency of the HCF loading further decreased the number of cycles to failure [2].

In [4–9] the effect of superimposed HCF cycles on fatigue crack growth was studied. For long cracks and small-scale yielding conditions, the HCF cycles lead to accelerated crack growth rates in comparison to pure LCF loading as soon as the total stress intensity range ΔK_{total} overcomes a certain threshold ΔK_{onset} [6,7,10]. ΔK_{onset} can usually be attributed to the point when the stress intensity range of the HCF cycles (ΔK_{HCF}) exceeds the threshold of fatigue crack growth ΔK_{th}. Larger ΔK_{HCF} at constant ΔK_{total} shift ΔK_{onset} to smaller values [4,5]. In Powell et al. [4] the influence of the number of HCF cycles per LCF cycle on fatigue crack growth was investigated systematically. No measurable fatigue crack growth acceleration was found for 1, 10 or 100 HCF cycles per LCF cycle. For 1000 HCF cycles or more, significantly higher crack growth rates were observed for stress intensity factors above ΔK_{onset}.

While the effect of superimposed HCF loadings on the growth of long cracks and elastic material behavior has been well documented in literature, up to now the effect of LCF/HCF interaction on microcrack growth under large plastic deformations has not been investigated in detail. In this paper naturally grown cracks are measured with help of the replica technique for both pure LCF and combined LCF/HCF loading. A model is presented, which accounts for the accelerated crack growth rates under LCF/HCF conditions.

2. Analytical model

2.1. Basic model

Experiments by Neumann [11] and others [12,13] suggest a correlation between the crack growth increment da/dN and the cyclic crack-tip opening displacement $\Delta CTOD$ for cracks under mode 1 loading. This leads to the following crack growth law:

$$\frac{da}{dN} = \beta \Delta CTOD, \tag{1}$$

where β is a proportionality constant.

* Corresponding author.
E-mail address: christoph.schweizer@iwm.fraunhofer.de (C. Schweizer).

0142-1123/
doi:10.1016/j.ijfatigue.2010.08.008

According to Shih [14] a simple relationship exists between the J-integral and the crack-tip opening displacement:

$$CTOD = d_n \frac{J}{\sigma_0}, \tag{2}$$

where σ_0 denotes the yield stress and d_n depends on the hardening behavior of the material. For power-law hardening materials the crack-tip fields are the Hutchinson, Rice and Rosengren (HRR) singular fields [15,16]. In this case d_n is a function of the Ramberg–Osgood hardening exponent n and was tabulated by Shih [17] for both plane strain and plane stress. The tabulated values for plane strain given by Shih [17] can be fitted with a third order polynomial function:

$$d_n = 0.78627 - 4.41692n + 6.11945n^2 - 4.2227n^3. \tag{3}$$

If cyclic material behavior is considered, the cyclic J-integral (ΔJ) has a solid mathematical foundation if the material shows Masing behavior [18]. All properties in Eq. (2) have to be replaced by their cyclic counterparts. Following Kumar et al. [19] and Heitmann et al. [20], ΔJ can be approximated by the sum of an elastic (or small scale yielding) and a plastic contribution. For a small semicircular crack with crack length a in a flat specimen under plane strain and mode 1 loading conditions, one obtains

$$\Delta CTOD = \frac{d_{n'}}{\sigma_{cy}} \left(1.45 \frac{\Delta\sigma_{eff}^2}{E} + 2.4 \frac{\Delta\sigma \Delta\epsilon_{pl}}{\sqrt{1+3n'}} \right) a, \tag{4}$$

where n' is the cyclic hardening exponent, σ_{cy} is the cyclic yield stress and E is Young's modulus. $\Delta\sigma$ and $\Delta\epsilon_{pl}$ are the stress and plastic strain range respectively. The second term in brackets was derived by He and Hutchinson [21] for a power-law hardening material in the fully plastic limit, but modified by a factor 1.25 to account for the fact that a surface crack is considered [22]. Crack closure is taken into account by the use of the effective stress range $\Delta\sigma_{eff} = \sigma_{max} - \sigma_{op}$ in the elastic part of ΔJ, as was proposed by Heitmann et al. [20]. σ_{max} and σ_{op} are the maximum and crack opening stress, respectively. All quantities in Eq. (4) can be determined from stress–strain hysteresis loops except σ_{op}, which can either be estimated with empirical formulas given in [20,23,24] or taken from numerical calculations. Here, the crack opening stress equation by Newman [23] is used, which predicts decreasing crack opening stresses with increasing maximum stresses, as is observed under LCF conditions [25].

The analytical expression for $\Delta CTOD$ (Eq. (4)) contains several assumptions. The interpolation formula for the cyclic J-Integral is an engineering approach for combined elastic and plastic deformations. Furthermore, the HRR-solution for d_n deviates from finite element calculations, if plasticity is not confined to a small zone around the crack-tip and the uncracked ligament is subjected primarily to tension. Thus, in [26] Eq. (4) was checked against results of finite element calculations. It was found that Eq. (4) agrees with the numerical calculations to within a factor of 1.25. In comparison to analytical expressions for stress intensity factors this deviation is rather large, but considering the above mentioned points, the authors believe that the accordance between Eq. (4) and the numerical results in [26] is good.

2.2. Model for combined LCF/HCF loading

To account for the effect of superimposed HCF loadings on fatigue crack growth, the basic model of the previous section is extended assuming that each HCF cycle leads to a change of the crack-tip opening displacement and according to Eq. (1) results in a crack growth increment $\frac{da}{dN}\big|_{\mathrm{HCF}}$. Thus, in one loading block, which comprises one LCF cycle and the corresponding superimposed HCF cylces (Fig. 1a), the total crack growth increment $\frac{da}{dN}\big|_{block}$ is expressed as the sum of the total (peak-to-peak) loading cycle and the sum of all HCF-cycles during one LCF cycle:

$$\left.\frac{da}{dN}\right|_{block} = \left.\frac{da}{dN}\right|_{total} + \sum_{block} \left.\frac{da}{dN}\right|_{\mathrm{HCF}}. \tag{5}$$

This summation is also employed by [4,6,7,9].

$\frac{da}{dN}\big|_{total}$ is calculated by using Eqs. (1) and (4), where all quantities from Eq. (4) are taken from the enveloping stress–strain hysteresis loop (Fig. 1a). In order to calculate the crack growth rates of the HCF cycles $\frac{da}{dN}\big|_{\mathrm{HCF}}$, $\Delta CTOD$ can again be calculated by Eq. (4), where now all quantities are taken from the stress–strain hysteresis loops of the HCF cycles. $\frac{da}{dN}\big|_{\mathrm{HCF}}$ only contributes, if the maximum stress of the individual HCF-cycle is larger than the opening stress σ_{op} from the enveloping hysteresis loop. In engineering applications the HCF loadings are typically so small that they result in elastic unloading from the enveloping stress–strain hysteresis loop as illustrated in Fig. 1a and in a stress intensity range ΔK_{HCF} close to the threshold of fatigue crack growth ΔK_{th}. In this case the second term in brackets in Eq. (4) vanishes and the effective stress range $\Delta\sigma_{eff}$ is evaluated by using the respective load ratio $\sigma_{min,\mathrm{HCF}}/\sigma_{max,\mathrm{HCF}}$ and the maximum stress of each HCF cycle. Additionally Eq. (4) is extended by a function G, which accounts for near threshold behavior [27].

$$\left.\frac{da}{dN}\right|_{\mathrm{HCF}} = (\beta \Delta CTOD) G. \tag{6}$$

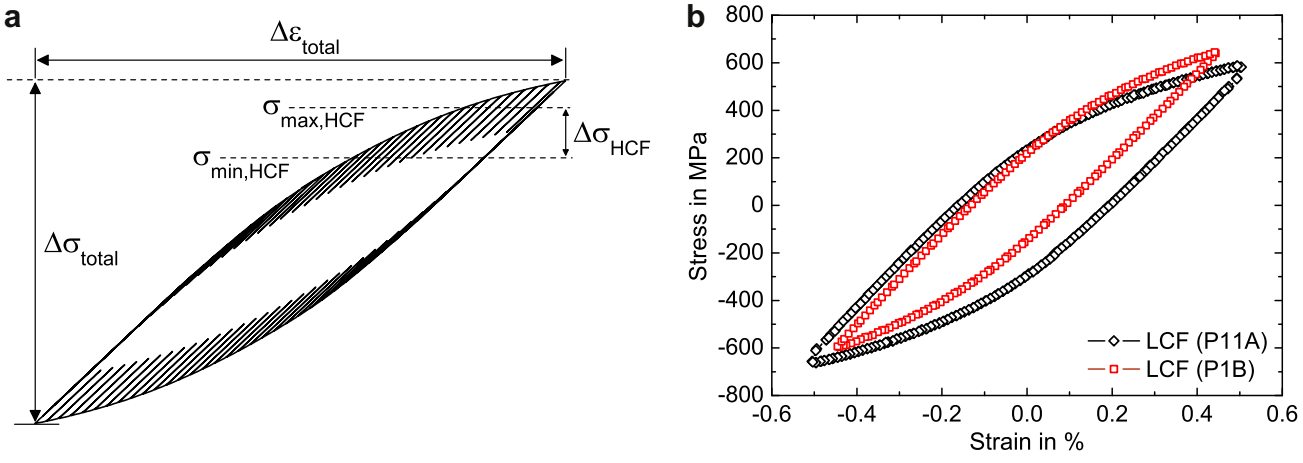

Fig. 1. (a) Schematic representation of a stress–strain hysteresis loop of one loading block of combined LCF/HCF loading. $\sigma_{max,\mathrm{HCF}}$ and $\sigma_{min,\mathrm{HCF}}$ are the maximum and minimum stresses of an arbitrary HCF-cycle. (b) Stabilized stress–strain hysteresis loops of specimens P11A and P1B for pure LCF loading.

The function G is defined as

$$G = 1 - \left(\frac{\Delta CTOD_{th}}{\Delta CTOD}\right)^{p/2} = 1 - \left(\frac{\Delta K_{th,eff}}{\Delta K_{eff}}\right)^{p}, \quad (7)$$

for $\Delta K_{eff} \geqslant \Delta K_{th,eff}$ and is set to zero otherwise. Here $\Delta K_{th,eff}$ denotes the effective threshold for fatigue crack growth and ΔK_{eff} is the effective stress intensity factor range. For elastic materials $\Delta CTOD$ is proportional to ΔK^2 and thus the original formulation of Newman [27] in terms of the stress intensity factor can be used. The exponent p controls the transition from the threshold to the Paris-line. Consistently with Eq. (4) the effective stress intensity factor range for a small semicircular surface crack in a flat specimen under mode 1 loading is taken from the solution of a penny-shaped crack, but modified by a factor of 1.12 in order to account for a surface crack [22]:

$$\Delta K_{eff} = 1.12 \frac{2}{\pi} \Delta\sigma_{eff} \sqrt{\pi a}. \quad (8)$$

3. Experimental details

3.1. Material

A 10%-chromium steel, which is used for turbine shafts served as a test material. The ferritic–martensitic microstructure is shown in Fig. 2. Single martensite needles are visible, which can be as long as 300 μm and often are arranged parallely in groups. Those needles are later found to have a significant influence on the initial stage of microcrack growth.

3.2. Experimental setup

A servohydraulic machine with a maximum force of 35 kN was used to perform the LCF and LCF/HCF tests. The fatigue specimens were cylindrical with a diameter of 7 mm in the gauge length and were polished. For displacement measurements an extensometer with a gauge length of 10 mm was employed. In the case of LCF/HCF interaction a sinusoidal displacement was superimposed with a frequency of 50 Hz. All tests were strain controlled and the LCF loadings were conducted under a strain ratio of $R_\epsilon = -1$ and with a strain rate of 10^{-3} s^{-1}. An overview over all LCF and LCF/HCF tests is given in Table 1, where $\epsilon_{a,LCF}$ and $\epsilon_{a,HCF}$ denote the strain amplitudes of the LCF and HCF cycles respectively.

Stabilized hysteresis loops from specimens P11A and P1B are shown in Fig. 1b. For specimens P12B and P09A, which were tested under combined LCF/HCF loading, the stress–strain response from specimen P1B corresponds to the enveloping hysteresis loop. The material parameters given in Table 2 were adjusted to the hysteresis loops from Fig. 1b.

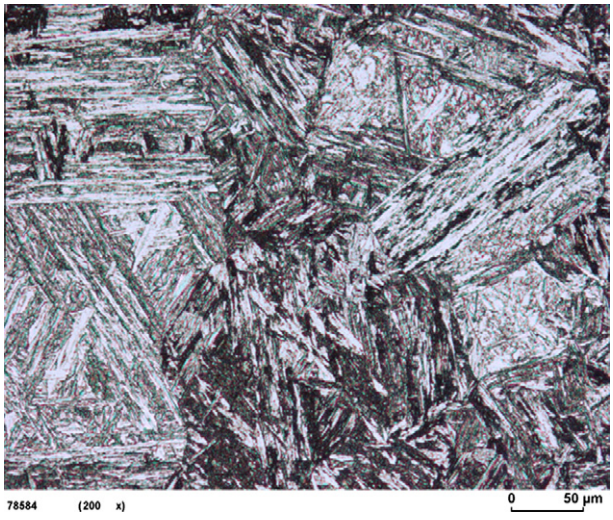

Fig. 2. Ferritic–martensitic microstructure of the 10%-chromium steel, which contains randomly distributed martensite needles.

Table 1
Overiew over all LCF and LCF/HCF tests.

Specimen	$\epsilon_{a,LCF}$ [%]	$\epsilon_{a,HCF}$ [%]
P1B	0.45	0
P11A	0.5	0
P12B	0.4	0.05
P09A	0.4	0.05

Table 2
Averaged material parameters determined from stabilized hysteresis loops.

E [MPa]	σ_{CY} [MPa]	n'
206,500	1213	0.163

3.3. Crack growth measurements

The fatigue crack length evolution of microcracks was followed by using the replica technique. To this end, the tests were interrupted after increments of 5% of the estimated total lifetime. A small force was applied in order to garantuee open crack faces when the replicas were taken. A acetate foil of 30 μm thickness was dissolved in propanone solution and was placed on the specimen surface. After drying, the foils, which contain the negative pattern of the crack on the surface of the specimen, were investigated by light microscopy. In the following the crack length a denotes half of the surface crack length observed, since semicircular surface cracks are typical for cylindrical smooth specimens.

4. Results

4.1. Microcrack growth under pure LCF loading

Specimen P1B was tested at a strain amplitude of $\epsilon_{a,LCF} = 0.45\%$. The two longest cracks were followed. Two replicas of crack 2 are shown in Fig. 3 at different stages of the total lifetime. The percentage of the total lifetime and the current surface crack length are given in the pictures. Crack 2 shows considerable stage 1 crack growth, reaching a surface crack length of 340 μm after 965 (LCF) cycles before kinking for the first time. In the following, the number of cycles refers to the number of LCF cycles, unless stated otherwise. The left side of Fig. 3 illustrates the crack shortly after the transition from stage 1 to stage 2 crack growth. In the following the crack deflects several times (see right side of Fig. 3). Crack 1 shows stage 1 crack growth until a surface crack length of 150 μm, followed by a stage 2 regime, which exhibits the same features as for crack 2.

The crack length evolution of both cracks is displayed in Fig. 4. The pronounced stage 1 crack growth of crack 2 is reflected in the higher crack growth rates until 965 cycles in comparison to crack 1. A kink in the crack length evolution clearly indicates the transition point from stage 1 to stage 2 crack growth.

The crack growth curves of Fig. 4 are supposed to represent the growth of individual cracks. However, the replicas reveal that coalescence of microcracks occurs. To illustrate this, two replicas of crack 1 at different stages of the total lifetime are shown in Fig. 5. The microcrack, which is visible on the top of the left side of the figure coalesces with the main crack during the following cycles. On the right side a detail of the crack-tip of crack 1 is shown

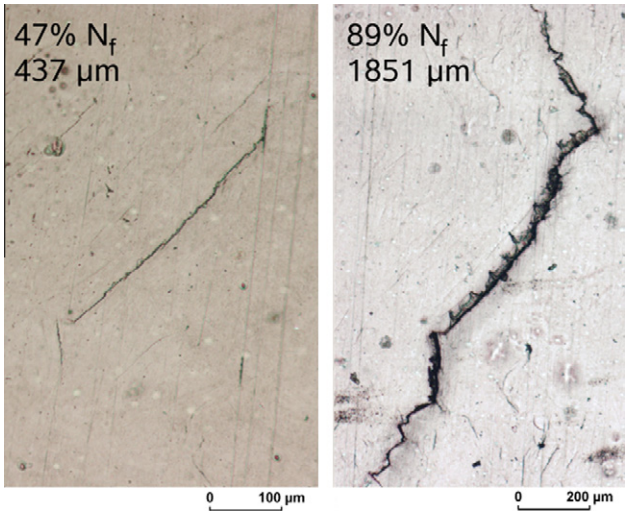

Fig. 3. Two replicas of crack 2 from specimen P1B after 1570 cycles (47% N_f) and 2973 cycles (89% N_f). The loading axis is in the horizontal direction. Additionally, the surface crack lengths are given in the pictures.

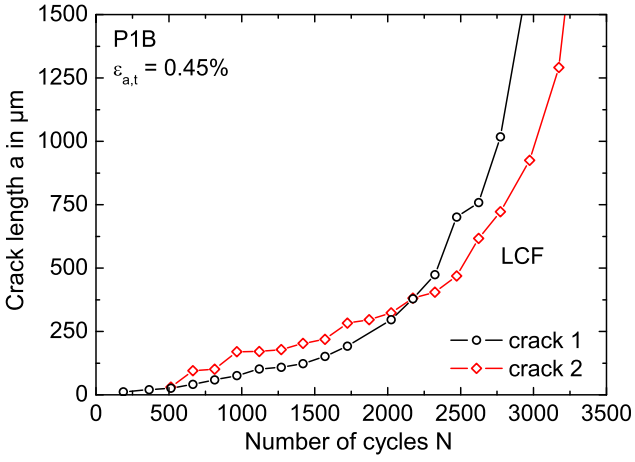

Fig. 4. Crack length evolution of two microcracks under LCF conditions for specimen P1B and $\epsilon_{a,LCF}$ = 0.45%.

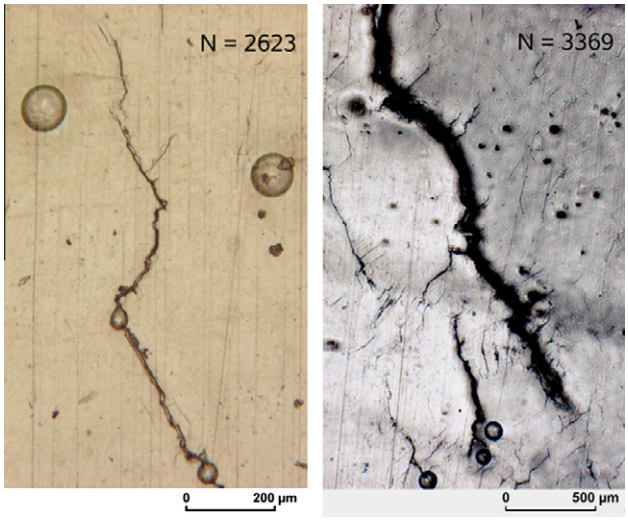

Fig. 5. Crack 1 from specimen P1B at different stages of the total lifetime. Both pictures show microcracks in the vicinity of the crack-tip. The crack density is much larger on the right side.

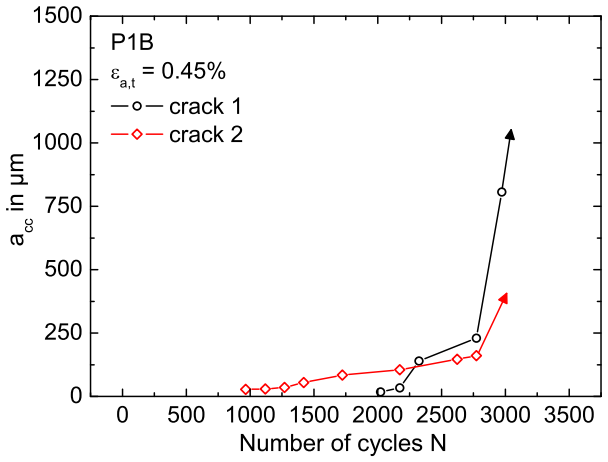

Fig. 6. Accumulated crack length due to crack coalescence. The arrows indicate that crack coalescence becomes increasingly important towards the end of lifetime. No data is available at large cycle numbers, since too many cracks coalesce between two replicas.

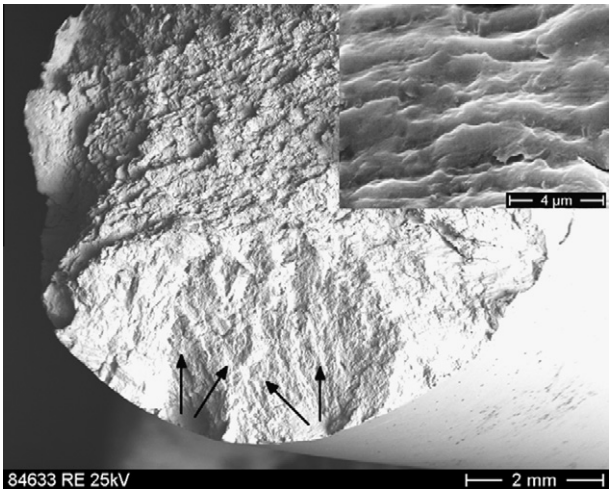

Fig. 7. Fracture surface of specimen P1B after final fracture. The striations are found 1 mm below the specimen surface. The arrows indicate the origins of two fatigue cracks.

at N = 3369 cycles. The crack density is obviously higher at this stage of the lifetime than on the left side of the figure. The detail of the crack on the left side of Fig. 5 is not visible on the right side of the figure.

Every time coalescence of microcracks with the main crack is observed, the length of the microcracks is measured separately and is accumulated over the number of cycles. This is done for both cracks 1 and 2 of specimen P1B. The resulting crack length is refered to as a_{cc} (cc: crack coalescence) and is shown in Fig. 6. For crack 1 no crack coalescence is observed until N = 2023 cycles, but a_{cc} becomes increasingly larger towards the end of the lifetime. At very large cycle numbers no reliable data is available, since too many cracks grow together within the interval between two replicas. To indicate this the arrows are shown in Fig. 6. For crack 2 crack coalescence is observed to occur earlier than for crack 1, but never contributes more than 1/4 to the total crack length in the regime considered.

Fig. 7 shows the fracture surface of specimen P1B. The fracture surface is rough but shows parts where striations are clearly visible. The striations shown in the figure originate from a point 1 mm below the specimen surface. The arrows mark the origin of two fatigue cracks, one of which being crack 1.

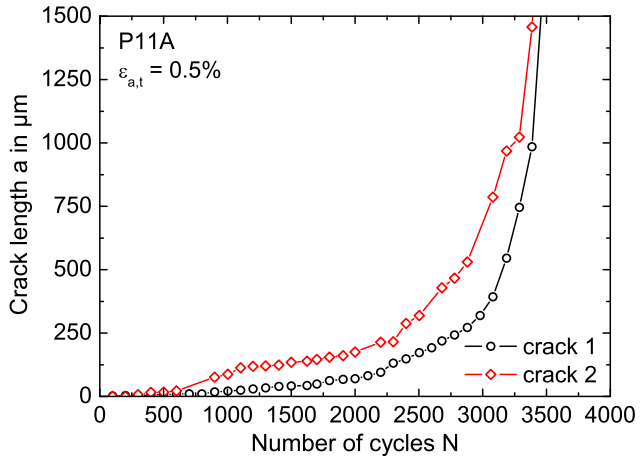

Fig. 8. Crack length evolution of two microcracks under LCF conditions for specimen P11A and $\epsilon_{a,LCF} = 0.5\%$.

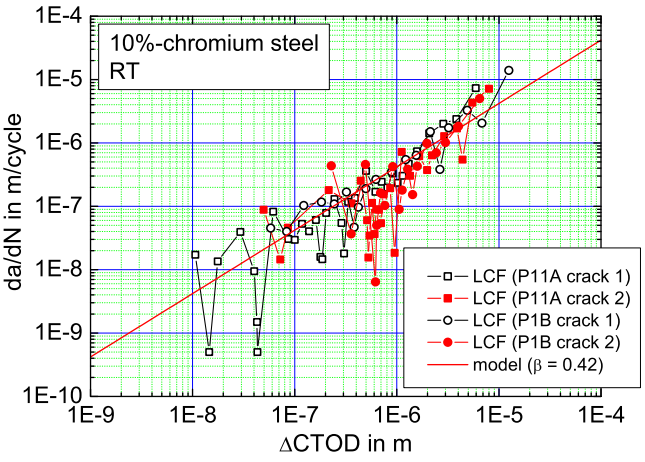

Fig. 9. Crack growth rates for all cracks under pure LCF loading. The line with $\beta = 0.42$ illustrates the linearity between da/dN and $\Delta CTOD$.

Specimen P11A was tested at a strain amplitude of $\epsilon_{a,LCF} = 0.5\%$ under pure LCF loading conditions. The two largest cracks, which lead to final rupture, are analysed and the crack lengths versus the number of cycles are shown in Fig. 8. Both cracks nucleate after only few percent of the total lifetime. Crack 1 grows perpendicularly to the loading axis throughout its lifetime, whereas crack 2 nucleates at a martensite needle and shows pronounced stage 1 crack growth until a surface crack length of 300 µm. This again leads to initially higher crack growth rates for crack 2.

Fatigue crack growth rates received from Figs. 4 and 8 are correlated in Fig. 9 with $\Delta CTOD$ from Eq. (4). The large scatter in the crack growth rates at low $\Delta CTOD$ values and small crack lengths is typical for microcracks. Crack 2 from specimen P11A and crack 2 from specimen P1B both show pronounced stage 1 crack growth before growing under stage 2. This is reflected in the crack growth rates, where a drop in da/dN is visible for both cracks at $\Delta CTOD \approx 6 \times 10^{-7}$ m (full symbols). This drop corresponds to the transition from stage 1 to stage 2 crack growth. To illustrate the linearity between da/dN and $\Delta CTOD$, Eq. (1) is fitted to the experimental data resulting in $\beta = 0.42$.

4.2. Microcrack growth under combined LCF/HCF loading

Specimen P12B was tested with the same total strain amplitude $\epsilon_{a,total} = \epsilon_{a,LCF} + \epsilon_{a,HCF} = 0.4\% + 0.05\%$ as specimen P1B. The two longest cracks are measured. Examplarily the replicas of crack 1 are displayed in Fig. 10. Crack 1 initially grows under stage 1 until a surface crack length of 150 µm (see left side of Fig. 10). In contrast to pure LCF loading, the crack stays almost perfectly in the plane perpendicular to the loading axis after the transition to stage 2 crack growth has occured (compare with right side of Fig. 10). Crack 2 emerges from three microcracks, which grow together during the initial stage 1 period. After crack coalescence the following growth is qualitatively the same as for crack 1.

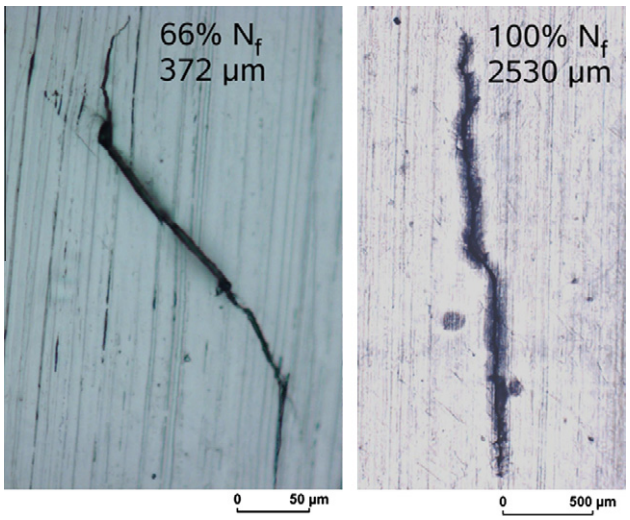

Fig. 10. Two replicas of crack 1 from specimen P12B after 1426 cycles (66% N_f) and 2150 cycles (100% N_f). The loading axis is in the horizontal direction. Additionally, the surface crack lengths are given in the pictures.

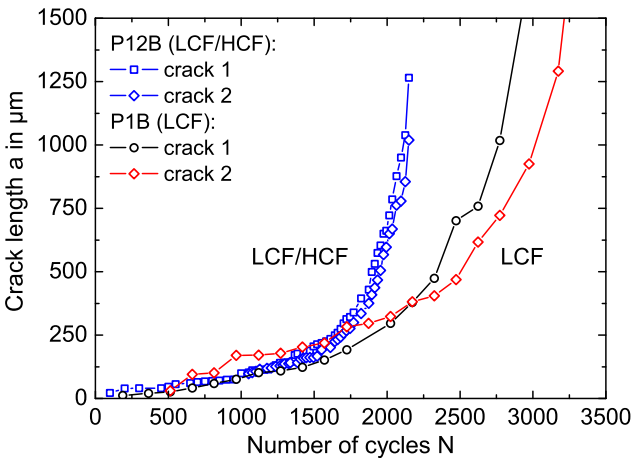

Fig. 11. Crack length evolution under LCF/HCF conditions in comparison to pure LCF loading.

In Fig. 11 the crack length evolutions under pure LCF loading and LCF/HCF interaction are compared. Initially the crack growth rates are almost identical for both loading conditions if crack 1 from specimen P1B is considered. When a crack length of approximately $a_{onset} = 100$ µm is reached, the LCF/HCF interaction leads to accelerated crack growth and a reduced lifetime in contrast to pure LCF loading. When crack 2 from specimen P1B is considered, the crack length a_{onset} cannot be identified that easily due to the pronounced stage 1 crack growth with initially higher crack growth rates.

Additionally, fractographic analysis are performed. The fracture surface of specimen P12B with a semicircular fatigue crack is

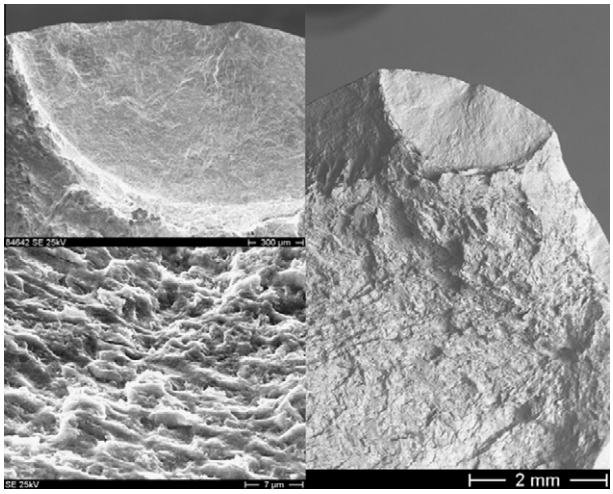

Fig. 12. Fracture surface of specimen P12B tested under LCF/HCF loading. The fracture surface is flat (right and upper left picture) and fatigue striations are visible (lower left picture), which stem from 1.1 mm below the specimen surface and have a spacing of approximately 3 µm.

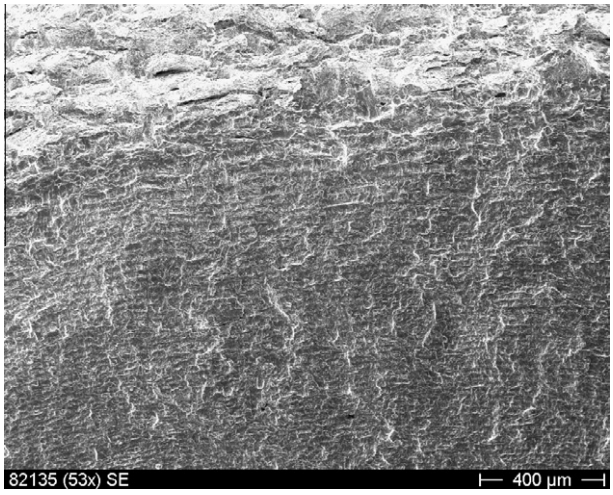

Fig. 13. Detail of the fracture surface of specimen P09A, which was tested under combined LCF/HCF loading. Striations are clearly visible in front of the transition to residual fracture.

shown in Fig. 12 and is much flatter than for pure LCF loading. The lower left side of Fig. 12 shows fatigue striations from 1.1 mm below the specimen surface with a spacing of approximately 3 µm. The fracture surface of specimen P09A, which is tested under exactly the same conditions as specimen P12B, is visible in Fig. 13. No replicas are taken in this case. Striations are clearly visible and are assumed to stem from one complete loading block. No substructure between the striations is found, which could be attributed to single HCF-cylces.

Crack growth curves for combined LCF/HCF loading are plotted in Fig. 14 together with the data from Fig. 9. In the case of the LCF/HCF loading $\Delta CTOD$ is taken from the enveloping hysteresis loop. While the LCF/HCF data (open triangles) seems to fall into the scatterband of the LCF data (black squares) for $\Delta CTOD < 3 \times 10^{-7}$ m, the HCF-cycles for larger $\Delta CTOD$ values lead to crack growth rates, which are approximately a factor of two higher than under LCF conditions. In addition, striation spacings from specimen P09A are displayed (open circles). At large values of $\Delta CTOD$ one striation spacing should correspond to the total crack growth increment of

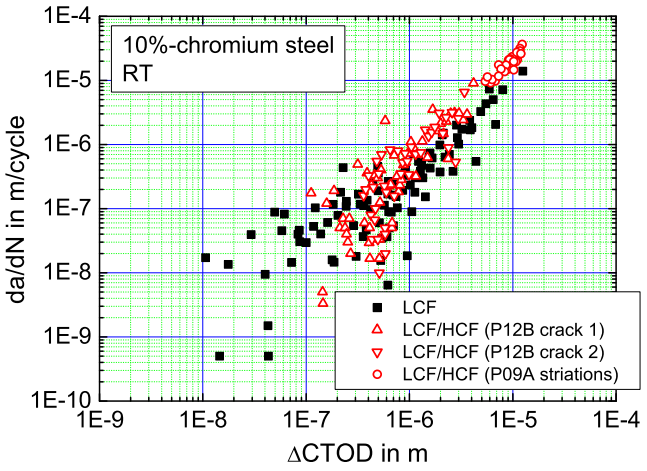

Fig. 14. Crack growth rates for LCF and LCF/HCF loading. Additionally, striation spacings are shown from specimen P09A.

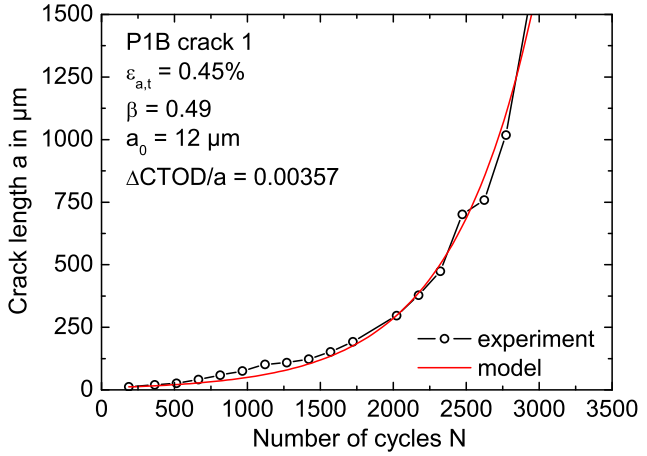

Fig. 15. Adjustment of the model to the experimentally observed crack length evolution under pure LCF loading conditions for specimen P1B and crack 1.

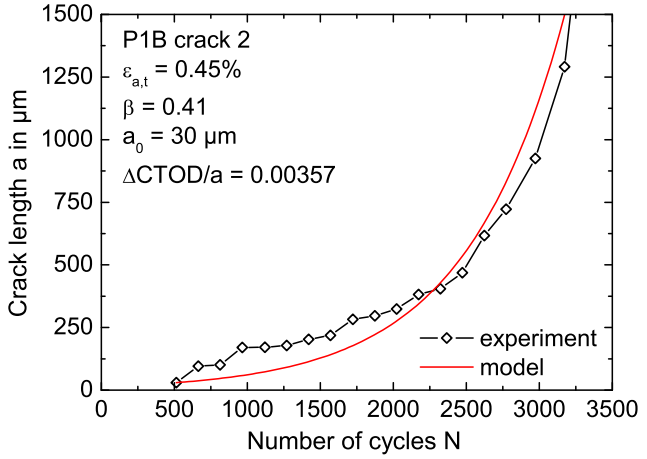

Fig. 16. Adjustment of the model to the experimentally observed crack length evolution under pure LCF loading conditions for specimen P1B and crack 2.

one LCF/HCF loading block. The striation spacings fall into the picture given by the crack growth rates. Unfortunately, no striations are visible at smaller crack depths. This probably stems from

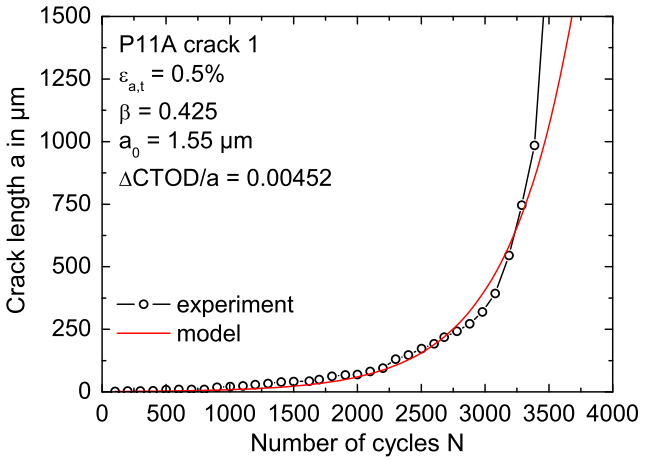

Fig. 17. Adjustment of the model to the experimentally observed crack length evolution under pure LCF loading conditions for specimen P11A and crack 1.

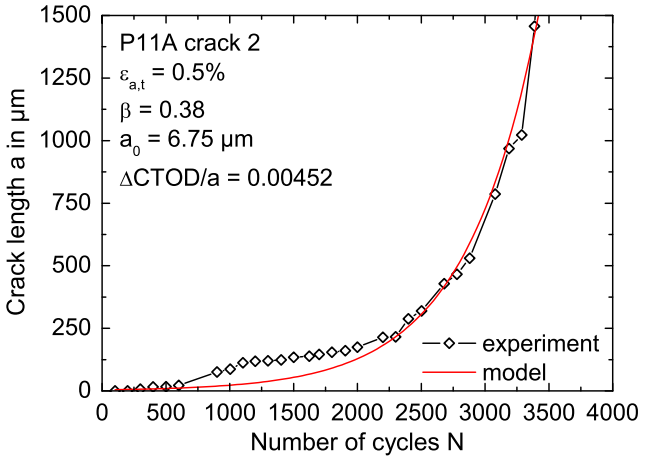

Fig. 18. Adjustment of the model to the experimentally observed crack length evolution under pure LCF loading conditions for specimen P11A and crack 2.

continuous crack closure such that the information on the fracture surface is partly destroyed.

4.3. Prediction of fatigue crack growth under pure LCF loading

For pure LCF loading the crack length is integrated from an initial crack length a_0 to an arbitrary crack length a by using Eqs. (1) and (4). This leads to the exponential crack growth law:

$$a = a_0 e^{\beta(\Delta CTOD/a)(N-N_0)}, \tag{9}$$

a_0 is set to the first crack length observed after N_0 cycles for each crack. Thus, the only unknown in Eq. (9) remains β, which is treated as a fitting parameter. The results are shown in Figs. 15–18. As long as stage 1 crack growth is not too pronounced, the model is capable of describing the observed crack length evolution (see Figs. 15 and 17). If this is not the case the model initially underestimates the measured crack lengths (see Figs. 16 and 18). The values for the proportionality constant β range from 0.38 to 0.49.

4.4. Prediction of fatigue crack growth under combined LCF/HCF loading

In order to desribe the LCF/HCF test, β is set to 0.49, which corresponds to the fitting result for crack 1 and specimen P1B and also

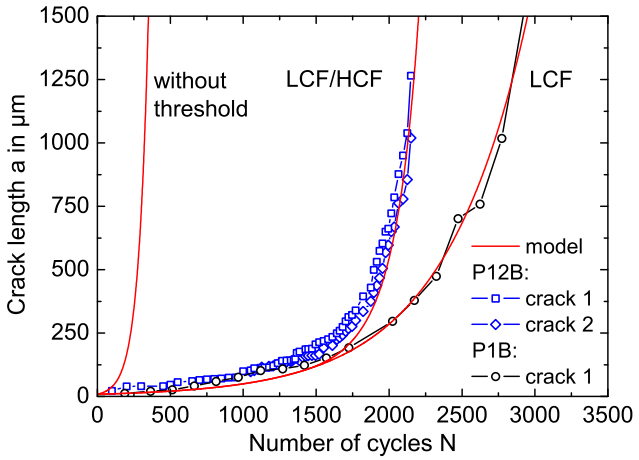

Fig. 19. Comparison between model and experiment for LCF/HCF interaction.

gives a good description for the crack growth curves from specimen P12B for $a < 100$ µm (Fig. 19). Now $\Delta K_{th,eff} = 2.6\,\mathrm{MPa}\sqrt{\mathrm{m}}$ is computed from Eq. (8), using the experimentally observed crack length of $a_{onset} = 100$ µm. This corresponds to a threshold in terms of $\Delta CTOD$ with $\Delta CTOD_{th} = d_{n'}\Delta K_{th,eff}^2(1-\nu^2)/(E\sigma_{CY}) = 9.19 \times 10^{-9}$ m. Here Poisson's ratio $\nu = 0.3$ is used. The exponent from Eq. (7) is set to $p = 0.3$, which is a typical value for steels. The model prediction is shown in Fig. 19. The model is able to describe the accelerated crack growth rates under combined LCF/HCF loading. To illustrate the importance of the threshold, the model prediction for the case that no threshold exists ($\Delta K_{th,eff} = 0\,\mathrm{MPa}\sqrt{\mathrm{m}}$) is also shown in the figure. The model then predicts rapid crack growth from the beginning resulting in a considerable underestimation of the lifetime.

5. Discussion

The microstructure of the ferritic–martensitic 10%-chromium steel contains long martensite needles, which are randomly distributed and can be as long as 300 µm (Fig. 2). In the uniaxial fatigue tests, some of the martensite needles are oriented under approximately 45° to the loading axis and thus experience the highest shear stresses. Those needles are likely to be responsible for the crack initiation and the distinct stage 1 crack growth with initially high crack growth rates. In some cases it is observed, that several microcracks nucleate at parallel martensite needles, which are situated very close to each other. In the following those microcracks grow together and the resulting single crack continues to grow. Whether the crack growth occurs along the phase boundaries of the martensite and the ferrite or in the martensite needle itself cannot not be clarified.

After the transition from stage 1 to stage 2 crack growth, the crack growth rate decreases and results in a drop of the da/dN curve (see Fig. 9 and crack 2 from P11A and crack 2 from P1B). It seems likely that the amount of roughness induced crack closure increases just after the transition from stage 1 to stage 2 crack growth and thus is responsible for the decreasing crack growth rates. After the crack has grown for a certain distance, the crack growth rates increase again. During the stage 2 regime crack coalescence with microcracks is sometimes observed and often seems to be responsible for the crack deflection under pure LCF loading. It is shown in Fig. 6 that crack coalescence is not dominant until the very last stage of the lifetime. During the final stage of the lifetime, the crack density increases considerably, and thus crack coalescence becomes more and more important.

Under pure LCF loading the fracture surface is rougher than under combined LCF/HCF loading. Obviously superimposed HCF-cycles force the crack to stay on the plane perpendicular to the loading axis. Striations are observed under both LCF and LCF/HCF loading conditions. This indicates that crack growth predominantly occurs by crack-tip blunting and resharpening as is implied by the $\Delta CTOD$ concept. Striation spacings are measured and compared to the crack growth rates received from the replicas. For combined low and high cycle fatigue loading, both crack growth rates and striation spacings indicate accelerated fatigue crack growth by approximately a factor of two in comparison to pure low cycle fatigue loading, as soon as a certain crack length is reached. This shows that fatigue crack growth rates received from the specimen surface can be related to the evolution of the crack depth in this case.

The model prediction for pure LCF loading is shown in Figs. 15–18. The model, which makes use of a linear correlation between da/dN and $\Delta CTOD$, is able to describe the microcrack length evolution as long as stage 1 crack growth is not dominant. This is the case for the cracks in Figs. 15 and 17. The agreement of the model and the experiments is somewhat surprising with regard to the very small crack lengths. Small cracks are often stopped at microstructural barriers such as grain boundaries, because the plastic zone cannot spread into the next grain. Under large plastic strains the plastic zone size is spread over the whole specimen and grain boundaries no longer pose barriers for microcracks in this sense. Further the model would imply a Paris-law of $da/dN \propto \Delta K^m$ with a Paris-exponent of $m = 2$ since $\Delta CTOD \propto \Delta K^2$. In the literature most Paris-exponents for metallic materials range between two and four. The 10%-chromium steel obviously has a slope which is close to $m = 2$, even though the scatter in data is large. For materials with $m \neq 2$, the model can be easily extended by introducing an exponent in Eqs. (1) and (6).

When stage 1 crack growth becomes more dominant, the model cannot capture the initially fast crack growth. The model does not include any mode 2 components, which cannot be neglected if the crack grows under 45° to the loading axis. A possible extension of the model taking into account mode 2 components could be formulated as follows: $da/dN = \beta(\Delta CTOD_I + \Delta CTOD_{II})$. Additionally, stage 1 cracks growing on a single slip system should show less plasticity induced crack closure as stage 2 cracks, since pure shear does not lead to opening components at the crack-tip. The crack opening stress equation by Newman [23] which is employed here, was developed for cracks under mode 1 loading and plasticity induced crack closure. Thus it does not contain any information about the difference between mode 2 and mode 1 controlled fatigue crack growth. This difference in the crack opening behavior for stage 1 cracks would result in larger effective cyclic J-integrals in Eq. (4) and hence also in larger crack growth rates. In order to properly describe the drop of da/dN after the transition from stage 1 to stage 2 due to roughness induced crack closure, complex numerical simulations are necessary, which are beyond the scope of this paper.

All values of the fitting parameter β lie between 0.38 and 0.49 and thus have a reasonable value in comparison with physical models of crack growth by crack-tip blunting. Since β is reasonably constant for different cracks and loading amplitudes, it could be used as a material constant for lifetime prediction models.

Under combined LCF/HCF loading accelerated crack growth rates are observed as soon as a certain crack length is reached. The model can describe this effect by introducing the effective fatigue threshold. The threshold can be roughly estimated from the crack length evolution and the resulting effective threshold $\Delta K_{th,eff} = 2.6\ \mathrm{MP}\sqrt{\mathrm{m}}$ corresponds to typical values for steels. Without the introduction of the threshold the model predicts much faster crack growth rates than what is observed in the experiments.

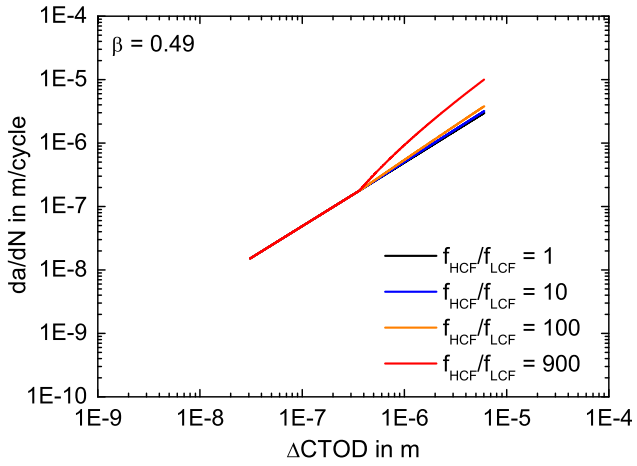

Fig. 20. Predicted influence of the HCF-frequency on da/dN. $\Delta CTOD$ is evaluated from the enveloping hysteresis loop.

The threshold is only introduced in the HCF-part of Eq. (5), since the applied LCF strain amplitudes even for crack lengths <10 μm result in a $\Delta CTOD$, which is larger than the threshold of $\Delta CTOD_{th} = 9.19 \times 10^{-9}$ m (Fig. 9).

It should be noted though that the point when the HCF-cycles become active is not clearly visible due to the larger scatter in fatigue crack growth rates for small cracks in comparison to typical long crack data. A possible solution would be to increase the total number of HCF-cycles during one loading block by either increasing the HCF frequency or extending the LCF cycle time. The currently used HCF frequency of 50 Hz with a cycle time of 18 s, results in 900 HCF-cycles per loading block. The effect of frequency on da/dN is studied in Fig. 20 using the adjusted model. For 1, 10 and 100 HCF-cycles per loading block, the acceleration in comparison to pure LCF loading is almost negligible. For $f_{HCF}/f_{LCF} = 900$, da/dN increases strongly above $\Delta CTOD = 3.6 \times 10^{-7}$ m. These findings qualitatively agree with the results found in Powell et al. [4], where it was found for long cracks that 1000 HCF-cycles per loading block were enough to clearly identify ΔK_{onset}, while $f_{HCF}/f_{LCF} \leqslant 100$ resulted in no measureable increase in fatigue crack growth rates. It has to be emphasized though that all HCF cycles were applied during a dwell time in tension only, whereas in the present study the HCF-cycles are active during the whole LCF-cycle. As was shown by Beck et al. [3] the damaging effect of the HCF-cycles during the compressive part of a TMF-cycle is only very small. This means that the amount of the damaging HCF-cycles per loading block is less than 1000 in our case. Considering the larger scatter in fatigue crack growth data for small cracks compared to the scatter for long cracks, it has to be concluded that more than 1000 HCF-cycles per loading block are desirable in future works to clearly identify the point, when the HCF-cycles become active. The proposed model for LCF/HCF describes the higher crack growth rates under LCF/HCF interaction. Still the model does not account for load interaction effects, which could strongly influence the crack opening stresses during a complete loading block. The use of a modified strip yield model as proposed in [27] or other simulation methods could give valueable information about the development of the crack opening stresses during one cycle.

6. Conclusions

In the present work the evolution of microcracks was followed for a ferritic–martensitic 10%-chromium steel by using the replica technique. Several cracks were observed under pure LCF and combined LCF/HCF loading. An analytical model was presented, which

accounts for accelerated crack growth rates under LCF/HCF conditions as soon as a certain crack length is reached.

The following conclusions can be drawn from this work:

- Long martensite needles were often responsible for the crack initiation and the following stage 1 crack growth regime for the 10%-chromium steel.
- Stage 1 cracks were found to reach surface crack lengths of more than 300 μm before kinking for the first time. Those cracks showed initially higher crack growth rates than cracks with less pronounced or no stage 1 regimes. After the transition to stage 2 a drop in the crack growth rates was observed.
- LCF/HCF interaction led to accelerated fatigue crack growth of microcracks in comparison to pure LCF loading as soon as a certain crack length was reached. This crack length could be identified with the point when the stress intensity of the HCF-cycles exceeded the threshold of fatigue crack growth for the first time. The resulting effective threshold of $\Delta K_{th,eff} = 2.6\ \mathrm{MPa}\sqrt{\mathrm{m}}$ corresponds to typical values for steels.
- The proposed model, which makes use of a linear correlation between da/dN and $\Delta CTOD$, can describe the crack length evolution under pure LCF loading if stage 1 crack growth is not too pronounced.
- The model can describe microcrack growth under LCF/HCF conditions and only needs few fitting parameters.

Acknowledgments

The authors thank the Stiftung Stahlanwendungsforschung im Stifterverband für die Deutsche Wissenschaft e. V. for the financial support of the present research. Special thanks to the study-group of the Forschungsvereinigung Verbrennungskraftmaschinen e. V. (FVV) for continuous and helpful discussions.

References

[1] Moalla M, Lang K-H, Loehe D. Effect of superimposed high cycle fatigue loadings on the out-of-phase thermal-mechanical fatigue behaviour of CoCr22Ni22W14. Mater Sci Eng A 2001;319–312:647–51.
[2] Beck T, Loehe D, Luft J, Henne I. Damage mechanisms of cast Al–Si–Mg alloys under superimposed thermal-mechanical fatigue and high-cycle fatigue loading. Mater Sci Eng A 2007;468–470:184–92.
[3] Beck T, Henne I, Loehe D. Lifetime of cast AlSi6Cu4 under superimposed thermal-mechanical fatigue and high-cycle fatigue loading. Mater Sci Eng A 2008;483–484:382–6.
[4] Powell BE, Duggan TV, Jeal RH. The influence of minor cycles on low cycle fatigue crack propagation. Int J Fatigue 1982;4:4–14.
[5] Powell BE, Duggan TV. Predicting the onset of high cycle fatigue damage: an engineering application for long crack fatigue threshold data. Int J Fatigue 1986;8:187–94.
[6] Powell BE, Hawkyard M, Grabowski L. The growth of cracks in Ti–6Al–4V plate under combined high and low cycle fatigue. Int J Fatigue 1997;19:167–76.
[7] Hall RF, Powell BE. Crack growth in imi 829 at 550 °C under combined high and low cycle fatigue. Mater High Temp 2002;19:1–8.
[8] Ding J, Hall RF, Byrne J, Tong J. Fatigue crack growth from foreign object damage under combined low and high cycle loading, Part I: experimental studies. Int J Fatigue 2007;29:1339–49.
[9] Hawkyard M, Powell BE, Hussey I, Grabowski L. Fatigue crack growth under the conjoint action of major and minor stress cycles. Fatigue Fract Eng Mater Struct 1996;19:217–27.
[10] Byrne J, Hall RF, Powell BE. Influence of LCF overloads on combined HCF/LCF crack growth. Int J Fatigue 2003;25:827–34.
[11] Neumann P. New experiments concerning the slip processes at propagating fatigue cracks. Acta Metall 1973;22:1155–65.
[12] Laird C, Smith GC. Crack propagation in high stress fatigue. Philos Mag 1962;7:847–57.
[13] Pelloux RMN. Crack extension by alternating shear. Eng Fract Mech 1970;1:697–704.
[14] Shih CF. Relationships between the *J*-integral and the crack opening displacement for stationary and extending cracks. J Mech Phys Solids 1981;29(4):305–26.
[15] Hutchinson JW. Singular behaviour at the end of a tensile crack in a hardening material. J Mech Phys Solids 1968;16:13–31.
[16] Rice JR, Rosengren GF. Plane strain deformation near a crack tip in a power-law hardening material. J Mech Phys Solids 1968;16:1–12.
[17] Shih CF. Tables of Hutchinson-Rice-Rosengren singular field quantities. Tech. rep. Brown University Report MRL E-147; 1983.
[18] Wuethrich C. The extension of the *J*-integral concept to fatigue cracks. Int J Fract 1982;20:35–7.
[19] Kumar V, German MD, Shih CF. An engineering approach for elastic–plastic fracture analysis. Tech. rep. Report NP-1931 on Project 1237-1 for Electric Power Research Institute, Palo Alto, California; 1983.
[20] Heitmann HH, Vehoff H, Neumann P. Advances in fracture research 84. In: Valluri SR, et al., editor. Proc of ICF6, vol. 5. Oxford and New York: Pergamon Press Ltd.; 1984. p. 3599–606.
[21] He MY, Hutchinson JW. The penny-shaped crack and the plane strain crack in an infinite body of power-law material. J Appl Mech 1981;48:830–40.
[22] Riedel H. Fracture at high temperatures. 1st ed. Berlin, Heidelberg, New York: Springer-Verlag; 1987.
[23] Newman JC. A crack opening stress equation for fatigue crack growth. Int J Fract 1984;24:131–5.
[24] Schijve J. Some formulas for the crack opening stress level. Eng Fract Mech 1981;14:461–5.
[25] Vormwald M, Seeger T. The consequences of short crack closure on fatigue crack growth under variable amplitude loading. Fatigue Fract Eng Mater Struct 1991;14:205–25.
[26] Schweizer C, Seifert T, Riedel H. Simulation of fatigue crack growth under large scale yielding conditions. J Phys: Conf Ser 2010;240:012043.
[27] Newman JC. A crack-closure model for predicting fatigue crack growth under aircraft spectrum loading. In: Chang JB, Hudson CM, editors. Methods and models for predicting fatigue crack growth under random loading, ASTM STP 748. American Society for Testing of Materials; 1981. p. 53–84.